Journal of Applied Geophysics 206 (2022) 104789

Contents lists available at ScienceDirect

Journal of Applied Geophysics

journal homepage: www.elsevier.com/locate/jappgeo

On the accuracy and spatial sampling of finite-difference modelling in discontinuous models

Saskia Tschache [a,b,*], Vetle Vinje [a], Einar Iversen [b]

[a] CGG Services (Norway) AS, Lilleakerveien 6A, 0216 Oslo, Norway
[b] Department of Earth Science, University of Bergen, P.O.box 7803, 5020 Bergen, Norway

ARTICLE INFO

Keywords:
Modelling
Seismic
Finite difference
Reflectivity method

ABSTRACT

Finite-difference modelling estimates the wavefield in the subsurface by solving the elastic or acoustic wave equation numerically in a discrete version of the subsurface. The derivatives in the wave equation are approximated by their finite-difference counterparts. In this paper, we investigate the accuracy of acoustic finite-difference modelling as a function of the spatial sampling rate, the frequency, the source-receiver offset and the model parameters and parametrisation. To represent discontinuities in a regular grid, we apply a tapered low-pass wavenumber filter to densely sampled compliance and density models using the Nyquist wavenumber of the desired grid as cut-off wavenumber. A long filter taper improves the finite-difference modelling accuracy but also leads to longer oscillations in the model grids. We use a 2D acoustic central-grid pseudospectral scheme and compare it to analytical solutions of the wave equation and the reflectivity method. We show that previous recommendations for the spatial sampling of four grid points per shortest wavelength in staggered-grid schemes also apply to central-grid schemes. In the case of a single thin layer, the accuracy of finite-difference modelling is dependent on the impedance contrast and the layer thickness. For accurate wide-angle reflection amplitudes of a thin layer with a strong impedance contrast, a denser grid sampling than four grid points per shortest wavelength is required. Furthermore, we demonstrate that the presented wavenumber filtering approach is better suited for the downsampling of regularly sampled compliance and density data derived from well logs than Backus averaging.

1. Introduction

Finite-difference (FD) modelling of seismic wave propagation is the engine of reverse time migration (RTM) and full-waveform inversion (FWI). It is also a valuable tool in the interpretation of seismic images. Because the FD technique finds wide application in the seismic industry, a thorough understanding of its accuracy is important.

Although most applications of seismic FD modelling, such as RTM and classical diving-wave FWI, are performed on models with relatively smoothly varying properties, realistic geological models often contain discontinuities. One example is the seabed that acts as a sharp contrast of acoustic impedance in marine seismic exploration (Yao et al., 2018). Additionally, strong guided waves resulting from the free surface and the fluid-solid boundary reflection can be produced in the water column. For instance, FWI in shallow-water North Sea data is challenged by water bottom reflections and guided waves (Raknes et al., 2015). Other examples of discontinuities encountered in seismic exploration are sediment-salt boundaries (Jones and Davison, 2014), basalt (Gallagher and Dromgoole, 2008), dolerite intrusions (Scheiber-Enslin et al., 2021), or thin layers (Juhlin and Young, 1993). Currently, FWI tends to produce models with high resolution so that the FD modelling is performed on models with more variations (Routh et al., 2017).

In this paper, we study the accuracy of acoustic FD modelling in the presence of discontinuities from a practical viewpoint. The focus is on the following research questions: How should discontinuous models be represented in regular grid models for FD modelling? What grid sampling is needed for an accurate modelling of models with a step, a thin layer or a stack of layers? Does the accuracy vary with offset? What consequences does a too coarse grid sampling have for the amplitude and phase of each frequency component? The answers to these questions give insight into the expected errors of acoustic FD applications and how to mitigate them.

Discontinuous (Aoi and Fujiwara, 1999) and adaptive (Pei et al., 2009) spatial grids and finite-element methods (De Basabe and Sen,

* Corresponding author at: CGG Services (Norway) AS, Lilleakerveien 6A, 0216 Oslo, Norway.
E-mail address: saskia.tschache@uib.no (S. Tschache).

https://doi.org/10.1016/j.jappgeo.2022.104789
Received 22 December 2021; Received in revised form 5 August 2022; Accepted 17 August 2022
Available online 22 August 2022

2007) have been proposed for accurate and efficient modelling of wave propagation in heterogeneous media. However, adaptive grids make the implementation more complex and come with challenges in data management, grid generation and high-performance computing (Zhang and Zhang, 2022). Typically, anisotropic acoustic modelling schemes on central, uniform grids are used in FWI (Warner et al., 2013; Agudo et al., 2018) and RTM (Zhang et al., 2011). We restrict our investigation to acoustic modelling on central, uniform grids without considering anisotropy.

Stephen (1983) and Levander (1988) compared FD modelling to the reflectivity method. They observed high agreement between these two modelling techniques when they were applied to a set of simple models provided suitable numerical parameters were chosen. However, a comparison for finely layered models has not, to our knowledge, been published before.

Gustafsson and Mossberg (2004) and Gustafsson and Wahlund (2004, 2005) analysed the errors associated with models containing discontinuities for time compact staggered-grid schemes of order two and four in both space and time. They showed that the error can be split into grid dispersion error and an interface error caused by a discontinuity. Grid dispersion can be controlled by using higher-order schemes in space (Gustafsson and Wahlund, 2005). Gustafsson and Wahlund (2004) demonstrated that the interface error is of first order even if the schemes they investigated had second- and fourth-order accuracy for smoothly varying model properties. Symes et al. (2008), and Symes and Vdovina (2009) estimated the interface error for a second-order in time and space staggered FD scheme and confirmed that the interface error is of first order. They observed a time shift proportional to the time step and the distance between the interface and the staggered computational grids. To summarize these observations, we can conclude that there are two types of errors, the error caused by grid dispersion and the interface error. While the grid dispersion can be controlled by higher-order schemes, the interface error is of first order in staggered-grid schemes irrespective of their order in space (Symes et al., 2008; Symes and Vdovina, 2009).

To increase accuracy, Moczo et al. (2002) constructed a heterogeneous staggered-grid scheme based on an averaged medium that represents a material discontinuity. Volume harmonic averaging of bulk and shear moduli and arithmetic averaging of density were applied. Lisitsa et al. (2010) and Vishnevsky et al. (2014) showed that second-order accuracy of common staggered-grid schemes could be preserved by applying such a parameter averaging.

Various methods have been proposed to reduce the interface error in central-grid schemes. Cohen and Joly (1996) achieved second-order accuracy for a fourth-order scheme by using an optimal averaging procedure based on plane-wave analysis. Zhang and Le Veque (1997) developed an immersed interface method to achieve second-order accuracy. Another member in the family of interface methods is the explicit simplified interface method proposed by Lombard and Piraux (2004).

Mittet (2017) studied the interface error in acoustic FD modelling using high-order and pseudospectral staggered-grid schemes. He observed that four points per shortest wavelength were required for spatial derivatives to avoid this type of error. In a related study, Mittet (2021a) confirmed that the pseudospectral method could only provide "half-spectral" accuracy in discontinuous media, in the sense that four instead of two points (corresponding to spectral accuracy) per shortest wavelength were required. This type of spatial aliasing error occurred also in high-order finite-difference schemes (Mittet, 2021a). In another study, Mittet (2021b) observed an accuracy limit of the order of 1/10 of the grid sampling interval for the implementation of interfaces by applying a band-limited Heaviside step function to the grids. In this way, even layers as thin as 1/1000 of the grid sampling interval could be represented properly leading to a small spectral amplitude error of $\pm 2.5\%$ and a negligible traveltime error. However, the experiments on thin-layer models were done in 1D and did not investigate the error for non-vertically incident waves. Staggered-grid high-order FD and pseudospectral schemes were used in these experiments.

The majority of studies analysed the interface error associated with staggered-grid schemes. However, many forward-modelling-based applications in the seismic industry use central-grid schemes that do not include special treatment of discontinuities. Central-grid schemes avoid numerical inaccuracies introduced by the interpolation necessary in staggered-grid schemes (Zhang et al., 2011). It is therefore important to investigate the interface error associated with central-grid schemes.

The cited studies restrict the numerical experiments to simple models for which the analytical solution exists. To go further, we use the reflectivity method as a reference to include thin-layer and multi-layer models. In this way, a better understanding of the accuracy of the FD method in more realistic scenarios can be gained.

In contrast to many other studies, we use a broadband wavelet with a uniform amplitude over a large frequency range to study the errors in amplitude and phase for each frequency component. Such an investigation yields more insight than a visual comparison of waveforms or simple error estimates as has been demonstrated by Mittet (2017, 2021a, 2021b). Furthermore, we study the variation of amplitude and phase errors with offset, which is especially relevant in the context of amplitude and phase variation with offset studies.

In this study, we compare the results of acoustic FD modelling to a true reference and investigate the interface error on simple (but not necessarily analytical) cases. In the simple case of a two-layer model, the analytical solution is computed by the Cagniard-de Hoop method (Cagniard, 1939, 1962; De Hoop, 1960). In multi-layer cases, modelling results of the reflectivity method (Fuchs and Müller, 1971; Müller, 1985; Kennett, 2009) serve as a reference. This modelling technique allows full-waveform modelling for horizontally layered media and is accurate for layers of any thickness (Daley and Hron, 1982). In order to save computation time in the FD modelling, the numerical experiments are done in 2D. The findings are still relevant for 3D modelling, since numerical errors persist when the dimensionality of the simulation is increased (Mittet, 2021a).

The paper is structured as follows: In section 2, we introduce the three modelling methods used in this study: the Cagniard-de Hoop method, the reflectivity method and the acoustic FD method. Another important aspect in section 2 is the preparation of grid models for FD modelling. In section 3, we analyse the accuracy of acoustic FD modelling results compared to the true reference for a step model, a thin-layer model and a realistic multi-layer model derived from a well log. Sections 4 and 5 are devoted to a discussion of the results and our conclusions for acoustic FD modelling in practice.

2. Methods

2.1. Cagniard-de Hoop method

The Cagniard-de Hoop method provides an analytical solution for wave propagation in stratified media. Diaz and Ezziani (2010) implemented this method for simple two-layer models and wave propagation in 2D (see Diaz and Ezziani, 2015). We used this code to calculate the analytical solution for the step model (section 3.1). Strictly speaking, the solution is quasi-analytical, since a numerical convolution is involved, but we refer to it as an analytical solution in this article.

2.2. Reflectivity method

We used the reflectivity method (RM) as the modelling technique for thin-layer and multi-layer models. The RM proved to be highly accurate when compared to the analytical solution computed by the Cagniard-de Hoop method for a step model.

Only the relevant principles of the RM are explained here and the reader is referred to Müller (1985) and Kennett (2009) for details. The RM is based on the Sommerfeld integral, which itself can be derived

from the Weyl integral for cylindrical symmetry (Müller, 2007). By the Sommerfeld integral, a spherical wave can be expressed as a superposition of conical waves (Aki and Richards, 2002). The RM was first proposed by Thomson (1950) and later developed by Fuchs and Müller (1971), Kennett (1979), Fryer (1980) and others. Typically expressed as a numerical integration over a part of the real and positive horizontal slowness axis, we found it beneficial to change the integration variable as proposed by Fuchs (1968). A review of the derivation of the relevant equations, which were used to produce the reference solutions for thin-layer and multi-layer modelling examples, is provided in Appendix A.

For the computation of synthetic seismograms in time, first the overall P-P reflectivity R_{PP} is computed by Kennett's method (Kennett, 1974) for a range of frequencies ω and angles of incidence θ to obtain $R_{PP}(\omega,\theta)$. This recursive computation involves the frequency-independent plane-wave reflection and transmission coefficients given by the Zoeppritz equations (Aki and Richards, 2002) as well as phase terms. The frequency dependency is introduced by those phase terms, which are responsible for correct traveltimes and interference of scattering. For a large number of layers, the task of computing $R_{PP}(\omega,\theta)$ is the most demanding in terms of computation time. In the next step, the integral over θ (see Eqs. (A.5) and (A.6)) is computed by numerical integration using the trapezoidal rule. In practice, the integrand should be inspected to find a suitable upper integration limit. Furthermore, a taper at the upper integration limit is recommended (Mallick and Frazer, 1987). After integration, a multiplication with the factors in Eqs. (A.5) and (A.6) including the source excitation function is performed. Finally, the inverse Fourier transform is used to compute the pressure signals in time.

By relationships between the source excitation $F(t)$ of an explosive pressure point or line source and the resulting waveform at any distance given by Müller (2007), it is possible to calculate the source function that gives rise to a desired wavelet at a specific distance from the source. In our modelling examples, we used the tapered Ormsby wavelet shown in Fig. 1. As a broadband wavelet with a flat amplitude spectrum over a wide frequency range, it allows us to analyse the interface error of each frequency component. The tapered Ormsby wavelet has the corner frequencies 6 Hz, 10 Hz, 100 Hz and 120 Hz, a peak time of 0.1 s, a duration of 0.2 s and a maximum amplitude of 1.

2.3. Finite-difference method

The 2D acoustic wave equation for pressure $P(\mathbf{x},t)$ at position $\mathbf{x}=(x,z)$ and time t is given by Eq. (1)

$$\kappa(\mathbf{x})\frac{\partial^2 P(\mathbf{x},t)}{\partial t^2}-\nabla\cdot\left(\frac{1}{\rho(\mathbf{x})}\nabla P(\mathbf{x},t)\right)=S(\mathbf{x},t), \tag{1}$$

where $\kappa(\mathbf{x})$ and $\rho(\mathbf{x})$ denote compliance and density, respectively, and $S(\mathbf{x},t)$ is the source term. The compressional wave velocity α is $\alpha=\sqrt{(\kappa\rho)^{-1}}$.

We used the Fourier method (Fornberg, 1975; Kosloff and Baysal, 1982), also called the pseudospectral method, where the spatial derivatives are computed in the Fourier domain. The spatial derivatives are exact up to the Nyquist wavenumber making a sampling of two grid points per shortest wavelength sufficient in theory.

For the time derivatives, a fourth-order finite-difference approximation (Etgen, 1986) was used. We used small time steps to ensure stability according to the Courant-Friedrichs-Lewy condition, avoid errors in the source injection, and to reduce temporal dispersion. The maximum relative dispersion error was computed to be $<10^{-5}$ so that a correction was not required.

The simulations were performed on a uniform, central grid. Perfectly matched layers as well as model extension were used at all model boundaries to avoid any model boundary reflections interfering with the target reflection signal.

2.4. Tapered low-pass wavenumber filtering of models

To find the optimal representation of a discontinuity in a regular grid, we devised an aliasing-protected algorithm similar to a procedure proposed by Mittet (2017). Starting from ideal models with sharp contrasts, very densely sampled models of P-wave velocity α and density ρ with a sampling interval of $\Delta z'$=0.001 m were created. In the next step, the compliance $\kappa=\rho^{-1}\alpha^{-2}$, the inverse of the bulk modulus, was computed.

The application of a non-windowed low-pass filter to the models would lead to long tails of Gibbs oscillations in the filtered models. These oscillations would be eventually sharply truncated at the model boundaries. Moreover, source and receivers would be located in a weakly varying medium instead of a homogeneous medium. In order to have a better control over the truncation and to understand its effect on the simulation result, we created a tapered low-pass filter. A window of length $N'\Delta z'=N\Delta z$ was defined, where Δz is the desired spatial sampling interval and N', $N>0$ are even numbers. The ideal filter coefficients f_j of a low-pass filter with the Nyquist wavenumber $k_{cut}=\frac{1}{2\Delta z}$ of the desired grid sampling as cut-off wavenumber represent a discrete sinc function, here expressed for $N'+1$ samples as

$$f_j=2k_{cut}\frac{sin\left(j\pi\frac{k_{cut}}{k_{Ny}}\right)}{j\pi\frac{k_{cut}}{k_{Ny}}}, \tag{2}$$

where $k_{Ny}=\frac{1}{2\Delta z'}$, $j=0,\pm1,\pm2,\ldots,\pm\frac{N'}{2}$. The filter coefficients f_j were multiplied by a flat-top window function w_j (D'Antona and Ferrero, 2006)

$$w_j=a_0-a_1cos\frac{2\pi\left(j+\frac{1}{2}N'\right)}{N'}+a_2cos\frac{4\pi\left(j+\frac{1}{2}N'\right)}{N'}-a_3cos\frac{6\pi\left(j+\frac{1}{2}N'\right)}{N'}+a_4cos\frac{8\pi\left(j+\frac{1}{2}N'\right)}{N'}, \tag{3}$$

where $a_0=0.21557895$, $a_1=0.41663158$, $a_2=0.277263158$, $a_3=0.083578947$, $a_4=0.006947368$, to create a tapered low-pass filter. This filter was applied to the densely sampled models V_i, $i=1,\ldots,L$ of compliance or density, respectively,

$$V_i^{filt}=V_i*\left(w_jf_j\right). \tag{4}$$

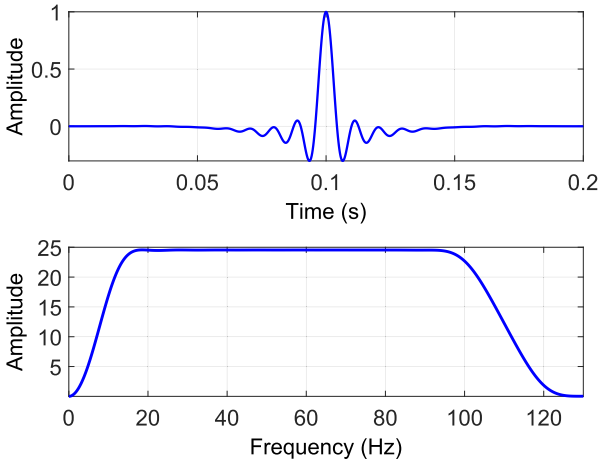

Fig. 1. Tapered Ormsby wavelet (top) used in all numerical experiments and its amplitude spectrum (bottom).

Finally, the densely sampled filtered model V_i^{filt} was resampled to the desired spatial sampling Δz. The velocity can then be computed from filtered compliance and density models.

Because of the application of a window function to the filter, only $N + 1$ grid points of the resampled model will be affected by a jump in a material property. Fig. 2 illustrates the tapered Gibbs oscillations for two different values of N. The windowing of the low-pass filter implies that the wavenumber filter has a less steep slope, i.e., its transition zone becomes wider as N becomes smaller. Hence, a limited portion of wavenumbers above the Nyquist wavenumber will remain after filtering. To evaluate the error associated with the tapering, we compared FD modelling results from tapered models with different window lengths $N\Delta z$ to modelling results from a non-tapered version. In this test, the source and receivers had a vertical distance of 500 m from the interface as shown in Fig. 3, so that the Gibbs oscillations have decayed almost entirely in the non-tapered version. We used a spatial sampling of $\Delta z = 2$ m. The L^2-norm error E was computed for each trace as

$$E = \frac{\sum_{l=0}^{S-1} \left(f_N(l\Delta t) - f(l\Delta t)\right)^2}{\sum_{l=0}^{S-1} \left(f(l\Delta t)\right)^2}, \tag{5}$$

where S is the number of trace samples, Δt the time sampling interval, f_N represents a trace modelled using a tapered model and f represents a trace modelled using a non-tapered model. In Fig. 2, the L^2-norm error averaged over all traces is given as an estimate of the error that is caused by applying the taper. Our numerical experiments showed that choosing N between 10 and 20 appeared to be a good trade-off to keep the Gibbs oscillations short and the taper-induced error low.

Fig. 4 illustrates how the location of the reflector relative to the grid determines where the filtered function is sampled. If the reflector is located at the centre of a grid cell, the maximum roughness of the Gibbs oscillation is captured (cf. Mittet, 2017) with the samples being located at the peaks and troughs of the oscillations as shown in Figs. 2 and 4d. If the reflector is located at the boundary of a grid cell (Fig. 4a), the samples are located close to the inflection points of the oscillations. We will investigate later what impact the interface location with respect to the grid has on the FD modelling result.

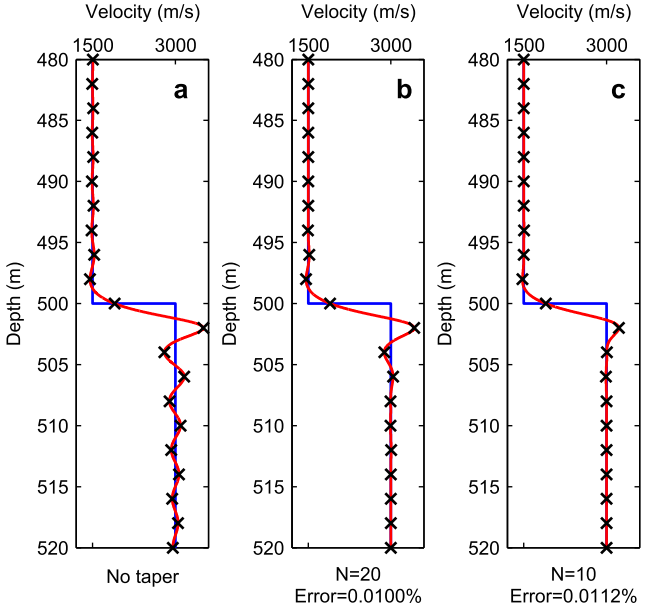

Fig. 2. Illustration of tapered low-pass wavenumber filtering of a 1D velocity step model. The densely sampled model (blue) is low-pass filtered (red) with a non-tapered filter (a) and tapered filters (b, c) so that N + 1 grid points are affected by the step. Black crosses show the grid samples with an interval of Δz = 2.0 m. Note that the Gibbs oscillations are asymmetric because the filtering is done in compliance and density. Average L^2-norm errors of FD modelling results caused by the taper are given below the plots. (For interpretation of the references to colour in this figure legend, the reader is referred to the web version of this article.)

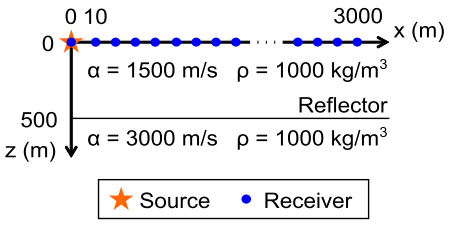

Fig. 3. Source and receiver locations in all modelling experiments. Receiver spacing is 10 m. Layer properties of the step model with constant density are given.

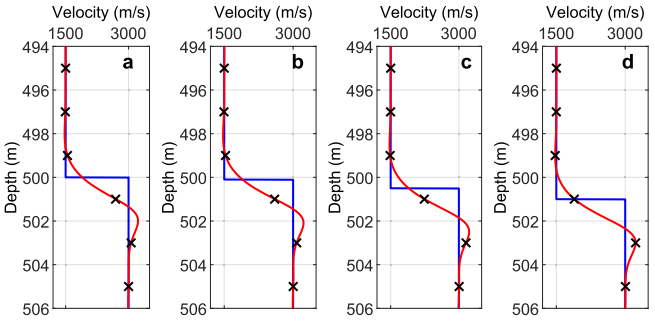

Fig. 4. Tapered low-pass wavenumber filtering of a 1D velocity step model with varying locations of the step relative to the grid. The densely sampled model (blue) is low-pass filtered (red) using a tapered filter of N = 10. Black crosses show the grid samples with an interval of Δz = 2.0 m. The step is located at z = 500.0 m (a), z = 500.1 m (b), z = 500.5 m (c) and z = 501.0 m (d), while the samples at z = 499 m, 501 m, etc. represent the centres of grid cells. (For interpretation of the references to colour in this figure legend, the reader is referred to the web version of this article.)

3. Results

3.1. Step model

In the first example of this study, we analyse the modelling error of the acoustic finite-difference (FD) method compared to the analytical solution for a single flat reflector. This reflector is located around 500 m below the source and receivers, which are all positioned at the same depth as visualised in Fig. 3. It separates two homogeneous half spaces with the properties given in Fig. 3. We applied the algorithm described above to create the grid models for the FD method using a taper of $N = 10$.

The direct wave was removed from all modelling results by subtraction. In this way, we can compare the single reflection event. We computed the normalised amplitude $R(\omega)$ and the phase difference expressed as the traveltime error $\Delta\tau(\omega)$ in milliseconds for a specific pair of source and receiver by Eqs. (6) and (7)

$$R(\omega) = \frac{A_{\mathrm{FD}}(\omega)}{A_{\mathrm{Ref}}(\omega)}, \tag{6}$$

$$\Delta\tau(\omega) = 1000\,\frac{\phi_{\mathrm{FD}}(\omega) - \phi_{\mathrm{Ref}}(\omega)}{\omega}, \tag{7}$$

where $A_{FD}(\omega)$ and $\phi_{FD}(\omega)$ denote the amplitude and phase spectrum of the FD signal and $A_{Ref}(\omega)$ and $\phi_{Ref}(\omega)$ denote the amplitude and phase spectrum of the reference signal, which is the analytical solution in this case.

3.1.1. Varying reflector location with respect to grid

In a first experiment, we analysed the impact of the reflector location with respect to the grid on the FD modelling accuracy. Fig. 5 illustrates various locations of an interface related to a grid cell of $\Delta x = \Delta z = 4.0$ m that is located between $z = 500$ m and $z = 504$ m. We tested four different reflector depths. At $z = 500$ m, the reflector is aligned with the boundary of a grid cell. At $z = 500.66$ m and $z = 501.33$ m, the reflector crosses a grid cell. At $z = 502$ m, the reflector is aligned with the centre of a grid cell. These locations can be expressed as 500 m + $a\Delta z$ depth with $a = 0$, $a = \frac{1}{6}$, $a = \frac{1}{3}$ and $a = \frac{1}{2}$. The amplitude and phase errors for these four scenarios are given in Fig. 6. It turns out that the best accuracy in terms of both amplitude and phase is achieved if the reflector is aligned with a grid cell boundary or, in other words, is located mid-way between two grid nodes. The largest error is observed if the reflector is located at the centre of a grid cell. This case represents the most challenging scenario and will be the focus of subsequent experiments to evaluate the accuracy of FD modelling. From Figs. 2 and 4, we can observe that the grid captures the maximum roughness of the Gibbs oscillations if the interface is located at the centre of a grid cell.

3.1.2. Varying grid sampling

Having identified the least and most challenging location of reflector position relative to the grid, we tested various grid samplings $\Delta x = \Delta z$ in these two locations using a taper size of $N = 10$. The normalised amplitude and traveltime errors are shown in Fig. 7. The Fourier method used in this study requires a spatial sampling of at least two grid points per shortest wavelength. With a maximum frequency of 120 Hz and a minimum velocity of 1500 m/s, the shortest wavelength is 12.5 m long. Theoretically, a grid sampling of 6.0 m should be sufficient to avoid grid dispersion. In the optimal case, where the interface is aligned with the grid cell boundaries, all tested grid samplings gave accurate modelling results. However, in the most challenging scenario, where the interface is aligned with the centres of the grid cells, the accuracy deteriorates with increasing frequency and grid sampling interval. We observe a slight amplitude loss in the high-frequency components for $\Delta x = \Delta z = 2.0$ m. This effect is even more dramatic for larger spatial sampling intervals. For $\Delta x = \Delta z = 3.0$ m, the amplitudes are reliable up to about 80 Hz. In the case of a grid sampling of 4.0 m, the limit is already reached at about 60 Hz and additionally a small phase error is observed at high frequencies. At long offset, that is, for wide-angle reflections, the amplitude and phase errors vanish for all tested grid sampling intervals. This observation is demonstrated by Fig. 8, which shows the normalised amplitude and traveltime error at 1000 m offset corresponding to an incidence angle of 45°.

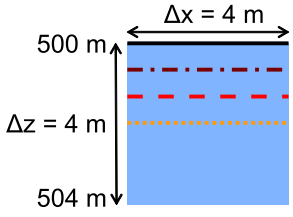

Fig. 5. Finite-difference grid cell (blue) of size Δx = Δz = 4.0 m and various reflector depths indicated by lines: z = 500.0 m (black, solid), z = 500.66 m (dark red, dash-dotted), z = 501.33 m (red, dashed) and z = 502.0 m (orange, dotted). (For interpretation of the references to colour in this figure legend, the reader is referred to the web version of this article.)

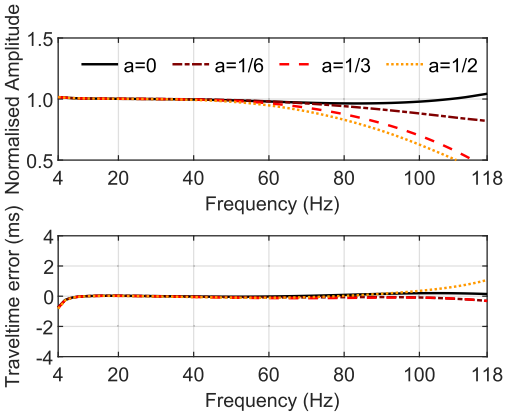

Fig. 6. Normalised amplitude (top) and traveltime error (bottom) of the reflection signal from a reflector at 500 m + $a\Delta z$ depth observed at 100 m offset and modelled by the acoustic FD method using a spatial sampling Δx = Δz = 4.0 m. The factor a determines the location of the reflector relative to the grid as shown in Fig. 5.

3.1.3. Varying taper size

The aim of our next experiment was to analyse the impact the taper, which is used in the wavenumber filtering of the grid models, has on the accuracy of the FD modelling results. We focus on the most challenging reflector location where it is aligned with the grid cell centres. Instead of using a taper size of $N = 10$, we increase N to 20 and 100, which means that longer tails of Gibbs oscillations away from the interface are included (see Fig. 2). The accuracy of the FD modelling results is shown in Fig. 9. Allowing more grid points to sample the Gibbs oscillations and represent the parameter jump improves the modelling results by shifting the amplitude accuracy limit to higher frequencies for each grid sampling. We observe that the limit is shifted up by about 20 Hz for $N = 20$ compared to the previous example where a taper of size $N = 10$ was used (Fig. 7, right). When using $N = 100$, highly accurate modelling results up to a grid sampling of 3.0 m are achieved. These results suggest that there is a trade-off between shortness of the operator containing the Gibbs oscillations on the one hand and required minimum grid sampling for full-bandwidth accuracy on the other.

3.1.4. Model grid in compliance vs. slowness

Another interesting question concerns which material property the tapered low-pass wavenumber filtering should be applied to in order to create the model grids. For this experiment, we added a jump in density from 1000 kg/m^3 to 2000 kg/m^3 at the same location as the velocity increase from 1500 m/s to 3000 m/s. We applied the tapered filter to compliance $\kappa = \rho^{-1}\alpha^{-2}$ (the inverse of bulk modulus) and density ρ (Fig. 10, left) and to slowness α^{-1} and density ρ (Fig. 10, right). The reflector was aligned with the grid cell centres to create the most challenging scenario. A taper of size $N = 10$ was used. Fig. 10 shows the normalised amplitude and traveltime errors for various grid sampling intervals. While performing the wavenumber filtering in slowness yields amplitude accuracy up to higher frequencies compared to the case of filtering in compliance, increasing phase errors occur with increasing spatial sampling. Already for a grid sampling of 2.0 m, a small traveltime error can be observed, which is present for all frequencies. The results suggest that using compliance results in best accuracy in phase, while using slowness results in best accuracy in amplitude. Note that slowness is not decoupled from density. It was demonstrated by Mittet (2017) that compliance and density are the best choice of material properties on which to perform the filtering operation. This observation is in agreement with the averaging derived by Backus (1962) and Moczo et al. (2002). We therefore decided to do the wavenumber filtering procedure in compliance and density in the subsequent tests.

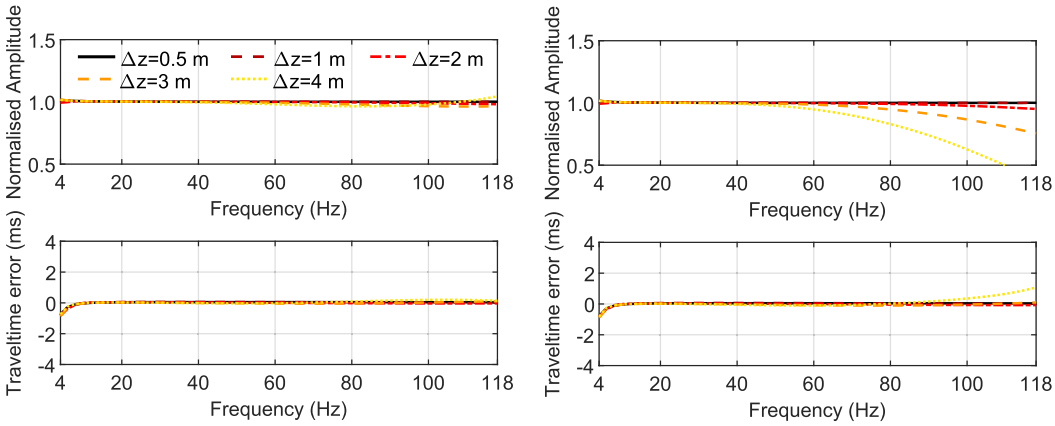

Fig. 7. Normalised amplitude (top) and traveltime error (bottom) of the reflection signal from a single reflector aligned with grid cell boundaries (left) and aligned with grid cell centres (right) observed at 100 m offset and modelled by the acoustic FD method using varying spatial sampling $\Delta x = \Delta z$.

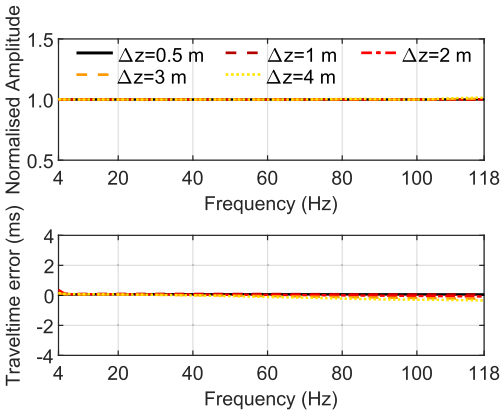

Fig. 8. Normalised amplitude (top) and traveltime error (bottom) of the reflection signal from a single reflector aligned with grid cell centres observed at 1000 m offset and modelled by the acoustic FD method using varying spatial sampling $\Delta x = \Delta z$.

3.2. Thin-layer model

In this experiment, we analyse the accuracy of the FD modelling of a reflection response from a thin, flat layer. The background model has a velocity of 1500 m/s and a density of 1000 kg/m^3. At a depth of about 500 m below the source and receivers (located as shown in Fig. 3), a thin layer with a thickness of 2 m, a velocity of 3000 m/s and a density of 2000 kg/m^3 was inserted. Wavenumber filtering and model sampling were performed in compliance and density using a taper size of $N = 10$. Similar to the previous examples, the direct wave was removed by subtraction prior to analysis of the reflection signal. The reference signal was calculated by the reflectivity method. The normalised amplitude of the FD modelling results and the traveltime error were computed by Eqs. (6) and (7).

With a thickness of 2 m and a velocity of 3000 m/s, the layer can be regarded as thin according to the Widess criterion of a thickness below $\lambda/8$ (Widess, 1973), where λ denotes the wavelength computed by the velocity of the thin layer and the maximum frequency of the wavelet. In such a case and opposite polarity reflectivity, the thin layer acts as an approximate time derivative operator to the wavelet. Fig. 11 illustrates how the initially flat spectrum is now altered such that there is a maximum amplitude at approximately 96 Hz. The figure also demonstrates the high accuracy of amplitudes for a grid sampling of up to 1.0 m and a weak amplitude loss for $\Delta x = \Delta z = 2.0$ m.

We investigated two different cases for the location of the thin layer with respect to the grid. In one case, the layer centre is aligned with a grid cell boundary, in the other case, it is aligned with a grid cell centre. Fig. 12 illustrates the velocity models after wavenumber filtering in compliance and density and the sample locations in these two cases for two different layer thicknesses. If the layer is centred at a grid cell boundary (Fig. 12a, c), the samples do not capture the maximum of the filtered function, but they capture the oscillations away from the layer. If the layer centre is aligned with the centre of a grid cell (Fig. 12b, d), the

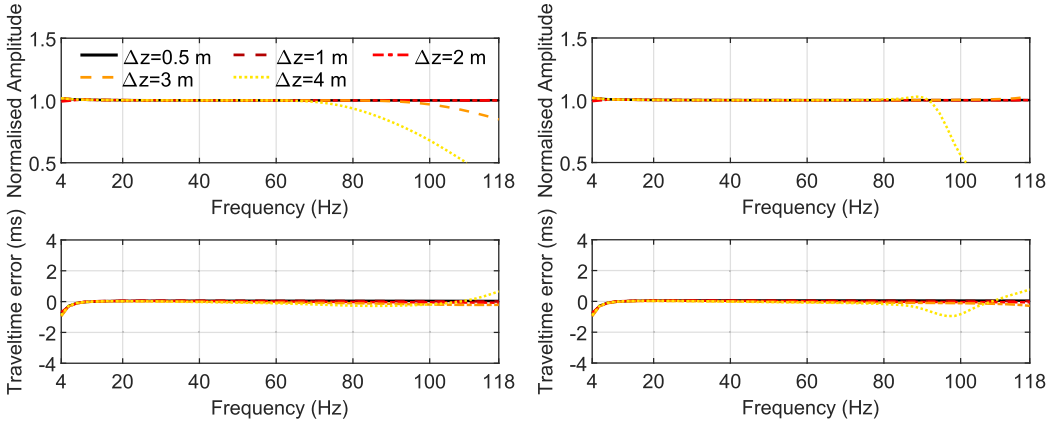

Fig. 9. Normalised amplitude (top) and traveltime error (bottom) of the reflection signal from a single reflector aligned with grid cell centres observed at 100 m offset and modelled by the acoustic FD method using varying spatial sampling $\Delta x = \Delta z$ and using a taper size of $N = 20$ (left) and $N = 100$ (right) to prepare the grids.

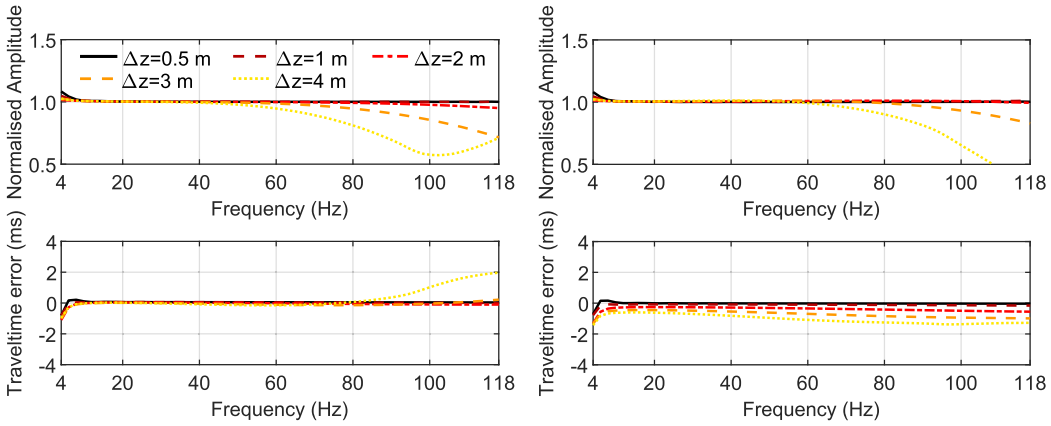

Fig. 10. Normalised amplitude (top) and traveltime error (bottom) of the reflection signal from a single reflector aligned with grid cell centres observed at 100 m offset and modelled by the acoustic FD method using varying spatial sampling $\Delta x = \Delta z$. Left: The discontinuity was filtered in compliance and density. Right: The discontinuity was filtered in slowness and density.

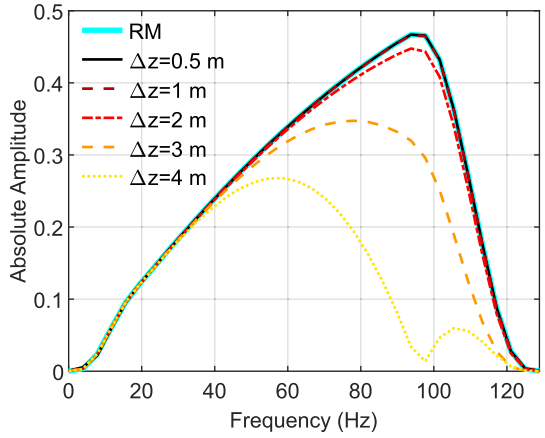

Fig. 11. Absolute amplitude of the reflection signal from a 2 m thick layer centred at grid cell boundaries observed at 100 m offset. The cyan graph shows the reference amplitude spectrum modelled by the reflectivity method (RM). The other graphs display the amplitude spectra of the acoustic FD modelling results using a varying spatial sampling $\Delta x = \Delta z$.

maximum of the filtered function is sampled, but the oscillations away from the layer are only weakly represented in the sample locations. Fig. 13 shows the normalised amplitude and traveltime error for varying spatial sampling if a 2 m thick layer is centred at grid cell boundaries and if its centre is aligned with grid cell centres.

For a thin layer, the FD modelling result is better if the layer centre is aligned with the centre of a grid cell. In this ideal case, full bandwidth accuracy up to $\Delta x = \Delta z = 3.0$ m can be achieved. By analogy with the step model, this is the case in which the oscillations represented by grid samples are the weakest. We have also seen that the maximum of the filtered velocity is captured by a sample, which supports amplitude accuracy. In the most challenging case where the layer is centred at the boundary of a grid cell, good accuracy is observed for the fine grid samplings of 0.5 m and 1.0 m. A weak amplitude loss occurs at the high-frequency components of the signal for $\Delta x = \Delta z = 2.0$ m, but the accuracy is still acceptable. For a larger spatial sampling, significant amplitude errors at high frequencies are seen. The traveltimes are correct except for $\Delta x = \Delta z = 4.0$ m above 95 Hz. It should be noted that the relative amplitude and phase errors seem to be large at low frequencies but are small in absolute values because the amplitudes are very low at such low frequencies (see Fig. 11).

Fig. 14 shows how the normalised amplitude varies with incidence angle for a layer thickness of 2.0 m (solid lines) and 0.2 m (dashed lines). In addition, an example with a weaker contrast in material properties is shown (dash-dotted lines). In this model, the velocity is increased by 200 m/s and the density is increased by 200 kg/m^3 in the 0.2 m thin layer. We used the most challenging scenario where the layer is centred at the grid cell boundaries and plotted the normalised amplitude at 60 Hz.

Unlike the step model, where amplitude and phase errors were reduced with increasing offset, in a thin-layer case, we observe an amplitude loss which increases as the angle of incidence or offset increases. This amplitude error is frequency-independent. It strongly depends on the layer thickness and the contrast in material properties. For all examples, we see that the amplitude error increases with increasing grid sampling. The results suggest that it is challenging to obtain an accurate amplitude variation with offset (AVO) response by FD modelling when very thin layers with strong contrasts in material properties are present. Traveltime errors were negligible in all shown examples.

3.3. Multi-layer model

After evaluating the accuracy of FD modelling for simple discontinuous models, we analysed the accuracy of the FD method in a more realistic model. At the same time, we compared the model downsampling by wavenumber filtering used in this study to the widely used Backus average (Backus, 1962). Based on well log data, we built a multi-layer model consisting of a stack of thin layers with a constant thickness of 0.2 m between 500 m and 600 m depth and extrapolated constant model properties upwards and downwards. We applied the tapered low-pass wavenumber filtering to the compliance and density models of the original sampling $\Delta z' = 0.2$ m to create models of sampling $\Delta z = 3.0$ m and $\Delta z = 4.0$ m using $N = 14$ and $N = 20$, respectively. An alternative approach to downsample densely sampled elastic properties is to use the Backus average. For our case of acoustic, isotropic layers, the equations reduce to an averaging of compliance and an averaging of density. Hence, for $\Delta z = 3.0$ m, 15 layers of thickness 0.2 m contribute to one sample point. For $\Delta z = 4.0$ m, averaging is done over 20 layers. Fig. 15 demonstrates that the resulting downsampled models of wavenumber filtering and Backus average are similar but not identical. It should be noted that the Backus averaging is only valid if Δz is much smaller than the seismic wavelength, that is, maximum 1/10 of the wavelength (Mavko et al., 2009). With the shortest wavelength being 15.5 m in this example, the criterion is not fulfilled for $\Delta z = 3.0$ m or larger.

Source and receiver locations are the same as in previous experiments (see Fig. 3). We used the reflectivity method to produce a reference dataset based on the original densely sampled model with $\Delta z' = 0.2$ m. Fig. 16 shows the FD modelling results for the model versions

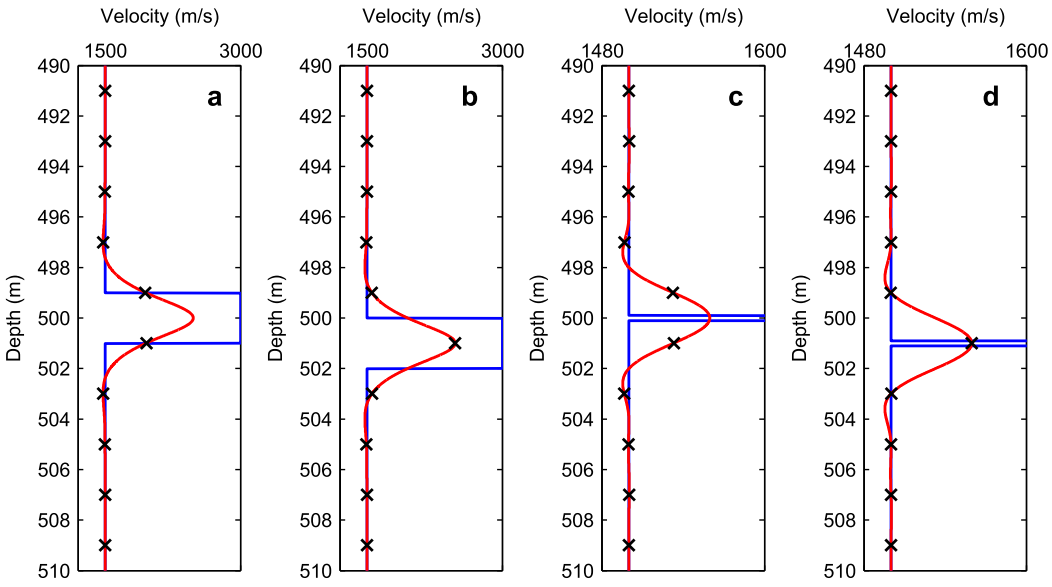

Fig. 12. Tapered low-pass wavenumber filtering of a 1D velocity model of a thin layer with increased velocity of 3000 m/s compared to the background velocity of 1500 m/s for varying locations of the layer centre relative to the grid. The densely sampled model (blue) is low-pass filtered (red) with a tapered filter of taper size $N = 10$. Black crosses show the grid samples with an interval of $\Delta z = 2.0$ m. a: 2 m thick layer centred at a grid cell boundary. b: 2 m thick layer centred at a grid cell centre. c: 0.2 m thick layer centred at a grid cell boundary. d: 0.2 m layer centred at a grid cell centre. The velocity axis is clipped in c and d. (For interpretation of the references to colour in this figure legend, the reader is referred to the web version of this article.)

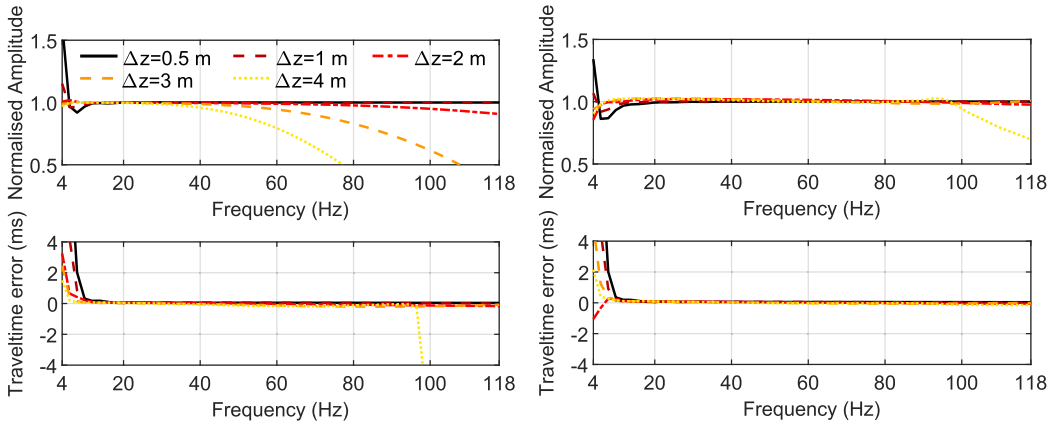

Fig. 13. Normalised amplitude (top) and traveltime error (bottom) of the reflection signal from a thin layer of 2 m thickness with its centre being aligned with grid cell boundaries (left) and grid cell centres (right) observed at 100 m offset and modelled by the acoustic FD method using varying spatial sampling $\Delta x = \Delta z$.

downsampled to $\Delta z = 3.0$ m compared to the reference dataset. The FD modelling results for the models resampled by the tapered low-pass wavenumber filter are in good agreement with the reference dataset and superior to the modelling results for the models produced by Backus averaging although differences are small. As noted before, the Backus average loses validity if the layer thickness becomes too large with respect to the wavelength.

Using a grid sampling interval of 4.0 m, which results in less than four points per shortest wavelength, yields poorer results as can be seen in Fig. 17. At short offsets, the high-frequency components of the FD modelling results based on the models produced by wavenumber filtering are too low in amplitude. At longer offset, the accuracy is satisfactory. As for 3.0 m sampling, the model created by Backus averaging leads to larger errors. The observations support the conclusion from the simple step model that four to five grid points per shortest wavelength are needed for full bandwidth accuracy. Similar to the step model, this requirement can be relaxed at long offsets.

4. Discussion

The reflectivity method can be regarded as a pseudo-analytical solution of the wave equation for layered models and has been used as a reference in other studies dealing with the accuracy of the FD method (Levander, 1988). By using the reflectivity method as a reference, we were able to analyse the offset-dependent accuracy of acoustic FD modelling for finely layered models.

Symes and Vdovina (2009) demonstrated that a discontinuity without special treatment leads to an interface error in finite-difference (FD) modelling. The interface error is purely in phase, thus, creating a time shift. It arises from misalignment between material discontinuities and computational grids. Mittet (2017) proposed the use of a band-limited Heaviside step function to properly implement a parameter jump in the simulation grid. The wavenumber limit is defined by the Nyquist wavenumber of the grid. By following this approach, the location of the interface is arbitrary and the phase error caused by

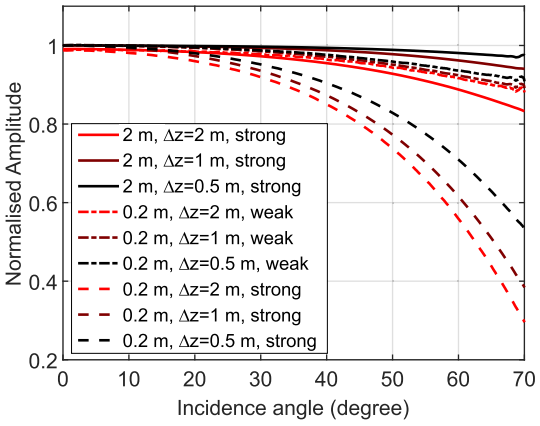

Fig. 14. Amplitude variation with incidence angle of the normalised amplitude at 60 Hz of the reflection signal from a thin layer for a varying spatial sampling $\Delta x = \Delta z$. Solid lines represent the example with a layer thickness of 2.0 m, dashed lines represent the example of a 0.2 m layer thickness and dash-dotted lines correspond to a 0.2 m layer thickness and a weaker contrast in acoustic impedance.

misalignment with the grid (when there is no special treatment of the interface) is corrected. In our study, we used a similar approach to limit the wavenumbers to the Nyquist wavenumber of the simulation grid. In all examples, we have shown that there is no phase error if discontinuities are filtered in compliance and density and the grid sampling is sufficiently fine.

Regarding the accuracy of amplitudes in the step-model example, we make similar observations to the staggered-grid observations of Mittet (2017, 2021a). For the general case, where the location of the discontinuity is not aligned with the grid, Mittet (2017) concluded from experiments using staggered-grid schemes that four to five grid points per shortest wavelength are required. In our experiments using a central-grid scheme, we observed that a spatial sampling of $\Delta x = \Delta z = 3.0$ m, corresponding to four grid points per shortest wavelength, is sufficient for accuracy in amplitude and phase when allowing $N + 1 = 101$ grid points to sample a discontinuity in material properties. Using a grid sampling of 4.0 m, corresponding to only 3 grid points per shortest wavelength, leads to inaccuracies in amplitude and phase for the high-frequency components. The amplitude error is dominant over traveltime error.

Reducing the taper size N shifts the accuracy limit for each grid sampling towards lower frequencies, so that a grid sampling of $\Delta x = \Delta z =$ 3.0 m is no longer sufficient for full bandwidth accuracy when $N = 20$ or $N = 10$. Using a small N makes the accuracy of the FD modelling more dependent on the location of the discontinuity relative to the grid. In agreement with Mittet (2017), we concluded that the most challenging scenario is reached when the interface is aligned with the centre of a grid cell. In such a situation, the grid samples capture the peaks and troughs of the Gibbs oscillations (see Fig. 4). An interesting observation is that the strict requirement concerning the number of grid points per shortest wavelength can be relaxed in the case of a wide-angle reflection from a single interface (see Fig. 8).

We have shown that the wavenumber filtering is ideally done in compliance and density for optimal accuracy. This choice is in agreement with the Backus average that reduces to an averaging in compliance and density for the isotropic, acoustic case and with the averaging proposed by Moczo et al. (2002).

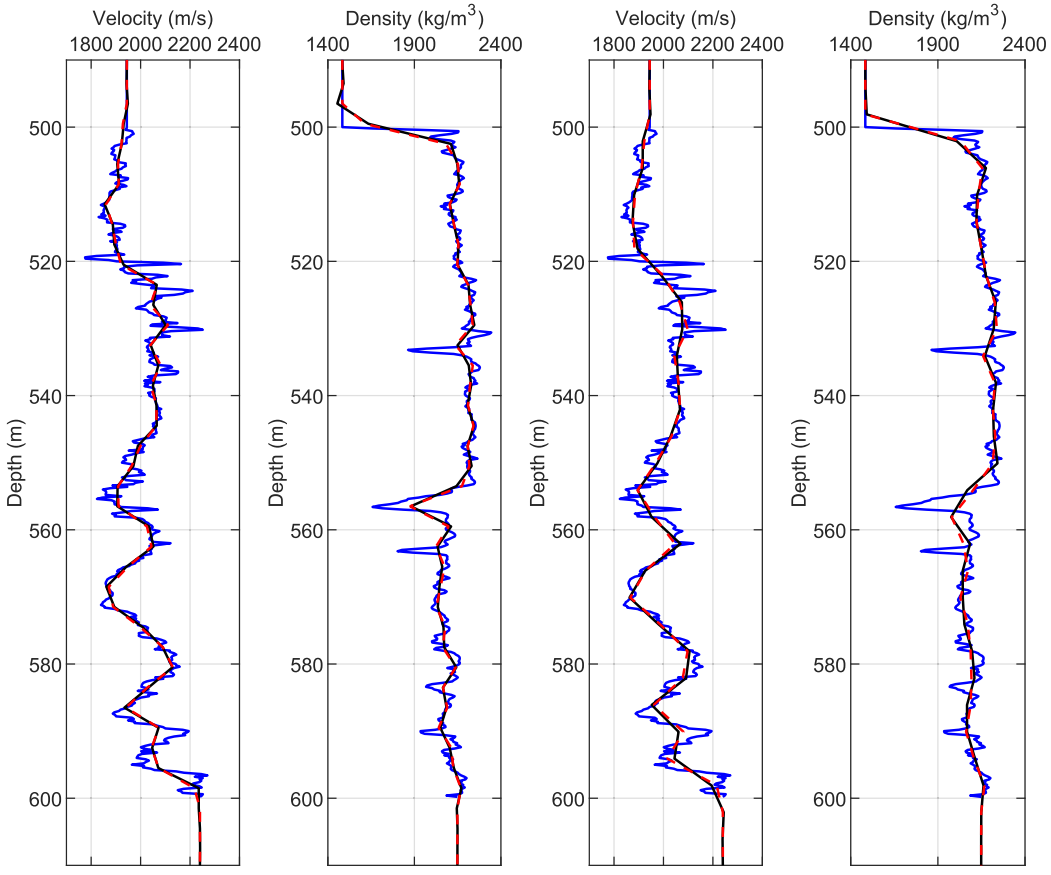

Fig. 15. Resampling of densely sampled models with $\Delta z' = 0.2$ m (blue, solid line) using Backus averaging (red, dashed line) and tapered low-pass wavenumber filtering (black, solid line). From left to right: velocity and density resampling to $\Delta z = 3.0$ m, velocity and density resampling to $\Delta z = 4.0$ m.

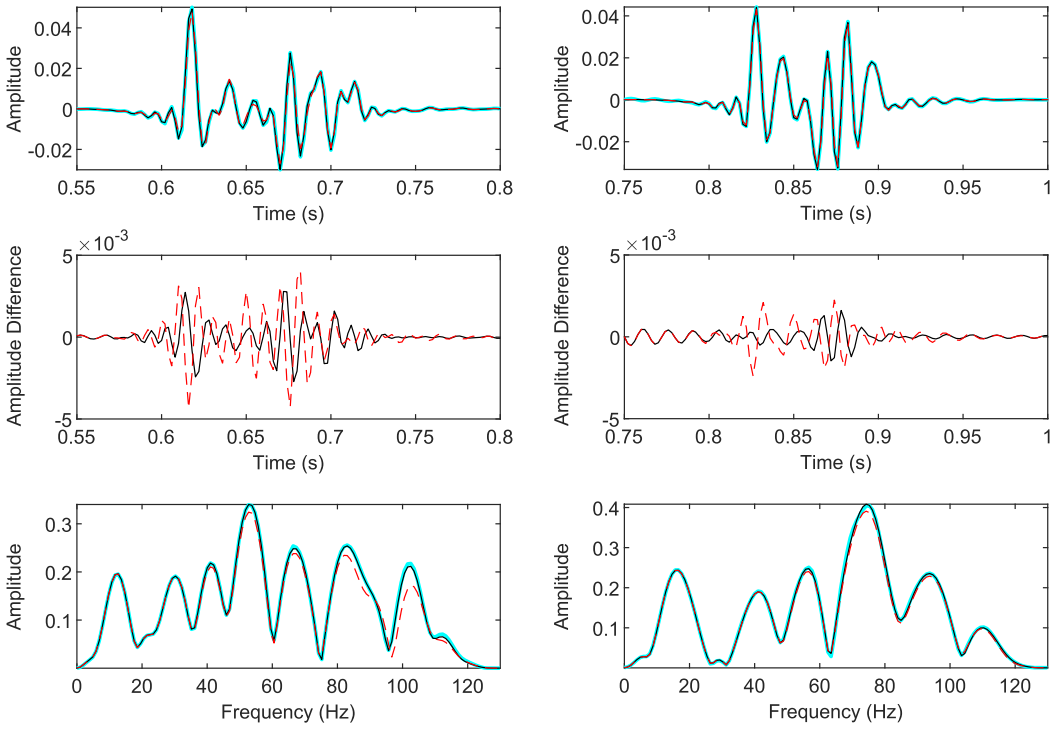

Fig. 16. FD modelling results (top) and corresponding amplitude spectra (bottom) for models downsampled from 0.2 m to 3.0 m spatial sampling by Backus averaging (red, dashed line) and tapered low-pass wavenumber filtering (black, solid line) compared to the reference dataset computed by the reflectivity method for the densely sampled model (cyan, solid line). The reflection response of the 500–600 m interval (Fig. 15) is shown after removal of the direct wave. Centre: difference between FD modelling results and reference. Left: observed at 100 m offset. Right: observed at 1000 m offset. (For interpretation of the references to colour in this figure legend, the reader is referred to the web version of this article.)

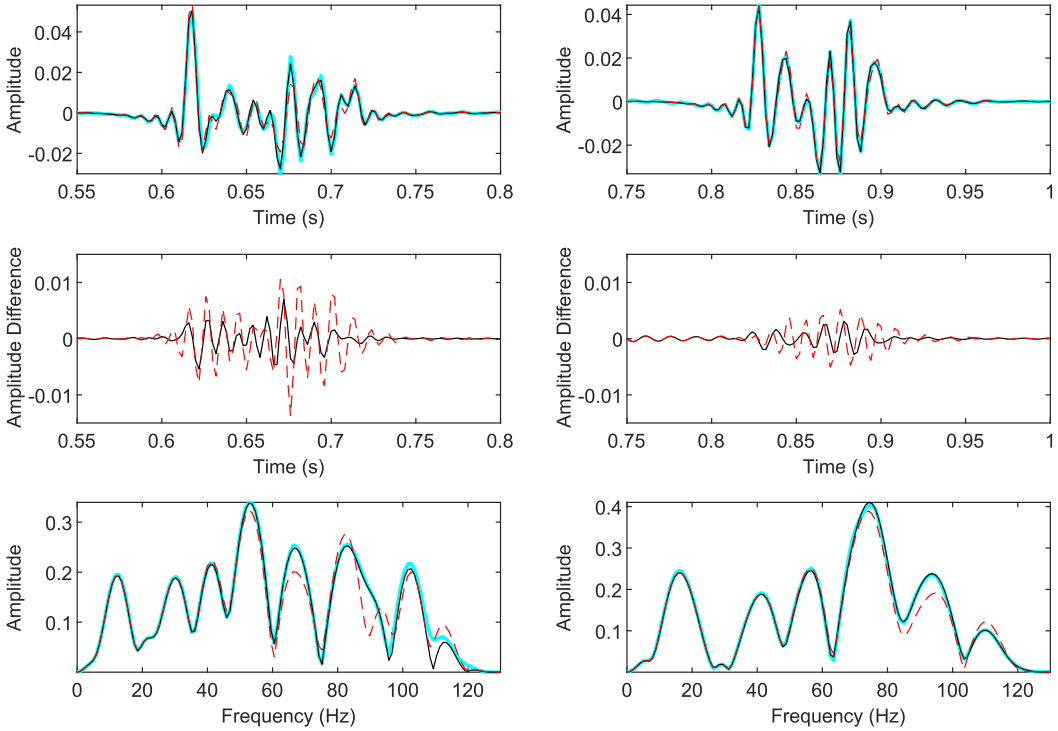

Fig. 17. FD modelling results (top) and corresponding amplitude spectra (bottom) for models downsampled from 0.2 m to 4.0 m spatial sampling by Backus averaging (red, dashed line) and tapered low-pass wavenumber filtering (black, solid line) compared to the reference dataset computed by the reflectivity method for the densely sampled model (cyan, solid line). The reflection response of the 500–600 m interval (Fig. 15) is shown after removal of the direct wave. Centre: difference between FD modelling results and reference. Left: observed at 100 m offset. Right: observed at 1000 m offset. (For interpretation of the references to colour in this figure legend, the reader is referred to the web version of this article.)

A typical application of these findings would be seabed reflections. Mittet (2021b) proposed a method to perform the parameter smoothing locally for continuous horizons. In this way, the seabed can be properly implemented in the simulation grid. With the right choice of taper size N and a grid sampling such that the requirement of four to five grid points per shortest wavelength is fulfilled, the seabed reflection will be accurate in amplitude and phase for the full bandwidth of the signal.

Although the tapered wavenumber filtering approach allows the representation of layers that are thinner than a grid cell, increasing amplitude accuracy problems were observed with increasing incidence angle, decreasing layer thickness and increasing contrast in material properties. Mittet (2021b) observed a slightly increased amplitude error but acceptable accuracy even for layers that were significantly thinner than a grid cell, e.g., an amplitude error of $\pm 2.5\%$ for a layer thickness 1/1000 of the grid step length. However, he did not investigate the offset-dependency of the amplitude error and used a considerably larger number of grid cells to capture the effect of a thin layer in the grid. Our results suggest that thin layers with strong parameter contrasts pose a challenge to the FD method, especially if an accurate amplitude variation with offset (AVO) response is needed. In such a case, decreasing the grid sampling further may help, as Fig. 14 suggests, but may also increase computational costs dramatically. Tests have shown that increasing the taper size N will only slightly reduce the amplitude error. Our work demonstrates that the reflectivity method provides a fast and efficient alternative for modelling the AVO effects of thin layers provided that lateral variations in material properties can be neglected. It should be noted that such extreme opposite polarity contrasts in acoustic impedance rarely occur in realistic subsurface models.

The multi-layer experiment confirmed that minimum four grid points per shortest wavelength are required to obtain an accurate FD modelling result. The model contains moderate contrasts in material properties such that the extreme case tested in the thin-layer example does not need to be considered. We have seen that the tapered low-pass wavenumber filtering in compliance and density yields similar results to averaging of compliance and density following the procedure proposed by Backus, adapted to acoustic and isotropic media. Mittet (2017) has already noted that the low-pass filtering in wavenumber domain resembles an averaging although there is no averaging done in the strict mathematical sense. For the downsampling of densely sampled models to build coarser regular grids for FD modelling, Backus averaging is not accurate enough because the spatial sampling becomes too large with respect to the wavelength. We have shown that the wavenumber filtering approach is a better alternative for such a case. Similar but more advanced downsampling methods were discussed by Capdeville et al. (2010) and Fichtner and Hanasoge (2017).

The experiments have shown that in the presence of discontinuities a finer grid sampling is required than for smooth models. Because our observations agree well with those of Mittet (2017, 2021a), we conclude that the recommendation of four to five grid points per shortest wavelength also apply to non-staggered, central-grid schemes, which are widely used in the seismic industry. This requirement assumes a proper representation of the discontinuity in the grid, limited to the Nyquist wavenumber of the grid. To achieve this, we used an adaptable wavenumber filtering procedure in compliance and density for optimal results. Although this representation of a discontinuity should guarantee invariance of the interface location relative to the grid, we observed that this was not generally the case when a taper was used with the filter. The most challenging situation for a single interface was created when the interface was aligned with the centre of a grid cell. For a single thin layer, the most challenging scenario was created when the layer was centred at a grid cell boundary. We have seen that the choice of taper size N affects amplitude accuracy. Allowing more grid cells to sample the Gibbs oscillations by choosing a larger N, generally improves accuracy. In other words, a coarser spatial sampling is then sufficient to achieve good accuracy for the full bandwidth of the signal. On the other hand, a large N creates models with wider zones of Gibbs oscillations, which might be unwanted. The parameter N allows easy adaption of the filter to specific needs.

The tapered low-pass wavenumber filtering of a finely sampled model as demonstrated here is a valid, effective and adaptable approach for models which vary only in one dimension. However, in the case of 2D or 3D models, this approach becomes computationally costly. Mittet (2021b) proposed a more efficient algorithm for continuous horizons. We agree with Mittet (2021a) that the study results for 2D wave propagation should also be applicable to 3D wave propagation. Similar numerical experiments for elastic, visco-elastic and anisotropic models are beyond the scope of this research, but the methodology and setup of the experiments presented in this paper will be useful for future studies on the topic. Mittet (2017) included an elastic example in his study and found that the same grid step was required as in the acoustic case, but higher wavenumbers had to be included in the grid generation. The consequences of the investigated inaccuracy of FD modelling in discontinuous models for applications such as full-waveform inversion and reverse time migration should be analysed in more detail in separate studies.

5. Conclusion

In this study, we investigated the accuracy of acoustic finite-difference modelling using the Fourier method for spatial derivatives when it is applied to a step model, a thin-layer model and a multi-layer model by comparing it to the analytical solution and modelling by the reflectivity method. The reflectivity method enabled us to extend existing studies that were restricted to simple models, where the analytical solution is available, and allowed us to study the accuracy of finite-difference modelling for finely layered models. We showed that previous recommendations for staggered-grid schemes to apply a low-pass wavenumber filter to densely sampled compliance and density models and to use a spatial sampling of minimum four grid points per shortest wavelength also apply to central-grid schemes. An exception are thin layers with very strong parameter contrasts, where the accuracy of finite-difference modelling deteriorates with increasing incidence angle. A denser spatial sampling is required in such a case. The presented aliasing-protected algorithm to represent discontinuities in a regular grid for finite-difference modelling includes an adaptable taper size. The taper size determines the steepness of the filter slope and the extent to which Gibbs oscillations are present in the model. Including more oscillations increases the accuracy. We have shown that this algorithm is better suited for the downsampling of densely sampled well logs for the finite-difference method than using Backus averaging.

Data availability statement

The data that support the findings of this study are available from the corresponding author upon reasonable request.

Declaration of Competing Interest

The authors declare that they have no known competing financial interests or personal relationships that could have appeared to influence the work reported in this paper.

Data availability

Data will be made available on request.

Acknowledgements

We are grateful to Volodya Hlebnikov, Peng Zhao and Thomas de Jonge for their assistance in running the numerical experiments. Jeremie Messud, Nabil Masmoudi, Rob Schouten and two anonymous reviewers are thanked for helpful comments to improve the manuscript.

Sara Pink-Zerling is thanked for proofreading. We would like to thank the developers of Gar6more2D for making their code available under a free software license. This work was funded by the Research Council of Norway under grant no. 310441.

Appendix A. Computing 2D pressure seismograms by the reflectivity method

To explain the theory of the reflectivity method, we assume a layered medium of plane horizontal, isotropic and homogeneous layers and cylindrical symmetry. We further assume that the first layer is a fluid and that the source and receivers are located in this layer, so that only P-waves are generated and measured. The source is assumed to be located at $z = 0$ and the z-axis is pointing downwards. To make the modelling comparisons easier, the free surface is not included here but could be implemented in general. Under these assumptions, we can express the incident and reflected wavefield from a point pressure source measured by a receiver at offset x and depth z in terms of the compression potentials Φ_{inc} and Φ_{refl} by eqs. (A.1) and (A.2), respectively (cf. Müller, 2007)

$$\Phi_{inc}(x,z,t) = \frac{1}{2\pi}\int_{-\infty}^{+\infty} \widehat{F}(\omega)e^{i\omega t}\int_0^{\infty} \frac{k_x}{ik_{z,1}}J_0(k_x x)e^{-ik_{z,1}|z|}\,dk_x\,d\omega, \tag{A.1}$$

$$\Phi_{refl}(x,z,t) = \frac{1}{2\pi}\int_{-\infty}^{+\infty} \widehat{F}(\omega)e^{i\omega t}\int_0^{\infty} \frac{k_x}{ik_{z,1}}J_0(k_x x)R_{PP}(\omega,k_x)e^{-ik_{z,1}|z|}\,dk_x\,d\omega, \tag{A.2}$$

where $\widehat{F}(\omega)$ denotes the Fourier transform of the source excitation function $F(t)$, t is time, ω is the angular frequency, k_x is the horizontal wavenumber, $k_{z,\,1}$ is the vertical wavenumber of the first layer, i is the imaginary unit, J_0 denotes the Bessel function of first kind and order zero, and $R_{PP}(\omega,k_x)$ denotes the complex overall P-P reflection coefficient of the stack of layers. It should be noted that $R_{PP}(\omega,k_x)$ is computed by an iterative scheme introduced by Kennett (1974) and contains all single and multiple reflections, mode conversions and evanescent waves. The phase terms in this computation lead to the frequency dependency. The outer integral in Eqs. (A.1) and (A.2) is an inverse Fourier transform back to the time domain while the inner integral is a Sommerfeld integral.

Following the derivations by Tsvankin (1995), the Sommerfeld integrals in Eqs. (A.1) and (A.2) can be expressed in terms of the departing or incidence angle θ instead of the horizontal wavenumber k_x by using the definition of the wavenumber k, the length of the wavenumber vector, $k = \frac{\omega}{\alpha_1}$ with α_1 being the P-wave velocity in the uppermost fluid layer. Using the following identities: $k_x = k\sin\theta$, $k_{z,\,1} = k\cos\theta$, $k_x dk_x = k^2\sin\theta\cos\theta d\theta$, we can now exchange the integration variable in Eq. (A.2) and find the Sommerfeld integral for the reflected wavefield to be

$$\widehat{\Phi}_{refl}(x,z,\omega) = -ik\widehat{F}(\omega)\int_{\Gamma} J_0(kxsin\theta)R_{PP}(\omega,\theta)e^{-ik|z|cos\theta}sin\theta\,d\theta. \tag{A.3}$$

The integration path Γ goes along the real axis from 0 to $\frac{\pi}{2}$ and then parallel to the imaginary axis from $\frac{\pi}{2}+i0$ to $\frac{\pi}{2}+i\infty$ in order to include homogeneous and inhomogeneous plane waves.

Using the derivations by Amundsen and Reitan (1994), we can transform Eq. (A.3) so that it gives the corresponding compression potential for a line source and 2D propagation instead of a point source and 3D propagation. This expression is relevant because we want to perform the numerical examples in 2D to save computational cost in the finite-difference modelling. The corresponding Eq. (A.4) for the potential in 2D is

$$\widehat{\Phi}^{2D}_{refl}(x,z,\omega) = -2i\widehat{F}(\omega)\int_{\Gamma} cos(kxsin\theta)R_{PP}(\omega,\theta)e^{-ik|z|cos\theta}\,d\theta. \tag{A.4}$$

Using the relationship between pressure P and compression potential Φ, $\widehat{P}(\omega) = \omega^2\rho_1\widehat{\Phi}(\omega)$ in a fluid with density ρ_1 (Müller, 2007), we can express the full reflection response of a stack of layers in pressure in the case of a line source (2D) and point source (3D) by the following Eqs. (A.5) and (A.6), respectively,

$$\widehat{P}^{2D}_{refl}(x,z,\omega) = -2i\omega^2\rho_1\widehat{F}(\omega)\int_{\Gamma} cos(kxsin\theta)R_{PP}(\omega,\theta)e^{-ik|z|cos\theta}\,d\theta, \tag{A.5}$$

$$\widehat{P}^{3D}_{refl}(x,z,\omega) = -ik\omega^2\rho_1\widehat{F}(\omega)\int_{\Gamma} J_0(kxsin\theta)R_{PP}(\omega,\theta)e^{-ik|z|cos\theta}sin\theta\,d\theta. \tag{A.6}$$

The corresponding horizontal and vertical displacement components, u_x and u_z, can be derived by taking the derivative of the potential Φ with respect to x and z, respectively. The incident wavefield in pressure can be derived from Eq. (A.1) in the same way as shown here for the reflection wavefield.

Typically, the reflectivity method is expressed using a limited integral over the horizontal wavenumber k_x or the horizontal slowness p, with $k_x = \omega p$ (Fryer, 1980; Aki and Richards, 2002). As can be seen from Eq. (A.2), the integrand attains very large values when the vertical wavenumber approaches zero. In general, poles that correspond to surface wave modes lie on the real k_x- or p-axis and hence on the integration path (Aki and Richards, 2002). These poles lead to difficulties in the numerical integration and to artefacts in the resulting synthetic seismograms. A common way to mitigate this difficulty is to introduce attenuation through complex velocities (see for example Müller, 1985). In our study, however, we wanted to compare to results from finite-difference modelling without attenuation and therefore needed a way to compute attenuation-free synthetic data by the reflectivity method. We found that changing the integration variable to the incidence angle θ is beneficial because the resulting integral no longer has a denominator that can approach zero (see Eqs. (A.3) to (A.6)). Several authors have made similar modifications to the traditional Sommerfeld integral (Fuchs, 1968; Fuchs and Müller, 1971). However, the expression of the Sommerfeld integral using the incidence angle is less advantageous if the method needs to be extended to anisotropic media. Note that the reflectivity method is a (visco-)elastic modelling tool, but acoustic modelling can be achieved by assuming very low S-wave velocities in all layers.

References

Agudo, Ò.C., da Silva, N.V., Warner, M., Morgan, J., 2018. Acoustic full-waveform inversion in an elastic world. Geophysics 83 (3), R257–R271. https://doi.org/10.1190/geo2017-0063.1.

Aki, K., Richards, P.G., 2002. Quantitative Seismology, 2nd ed. University Science Books, Sausalito, Calif.

Amundsen, L., Reitan, A., 1994. Transformation from 2-D to 3-D wave propagation for horizontally layered media. Geophysics 59 (12), 1920–1926. https://doi.org/10.1190/1.1443579.

Aoi, S., Fujiwara, H., 1999. 3D finite-difference method using discontinuous grids. Bull. Seismol. Soc. Am. 89 (4), 918–930. https://doi.org/10.1785/BSSA0890040918.

Backus, G.E., 1962. Long-wave elastic anisotropy produced by horizontal layering. J. Geophys. Res. 67 (11), 4427–4440. https://doi.org/10.1029/JZ067i011p04427.

Cagniard, L., 1939. Réflexion et Réfraction des Ondes Séismiques Progressives. Gauthier-Villars, Paris.

Cagniard, L., 1962. Reflection and Refraction of Progressive Seismic Waves. McGraw-Hill, New York.

Capdeville, Y., Guillot, L., Marigo, J.-J., 2010. 1-D non-periodic homogenization for the seismic wave equation. Geophys. J. Int. 181 (2), 897–910. https://doi.org/10.1111/j.1365-246X.2010.04529.x.

Cohen, G., Joly, P., 1996. Construction and analysis of fourth-order finite difference schemes for the acoustic wave equation in nonhomogeneous media. SIAM J. Numer. Anal. 33 (4), 1266–1302. https://doi.org/10.1137/S0036142992246445.

Daley, P.F., Hron, F., 1982. Ray-reflectivity method for SH-Waves in stacks of thin and thick layers. Geophys. J. Int. 69 (2), 527–535. https://doi.org/10.1111/j.1365-246X.1982.tb04963.x.

D'Antona, G., Ferrero, A., 2006. Digital Signal Processing for Measurement Systems: Theory and Applications. Information Technology: Transmission, Processing, and Storage. Springer, New York.

De Basabe, J.D., Sen, M.K., 2007. Grid dispersion and stability criteria of some common finite-element methods for acoustic and elastic wave equations. Geophysics 72 (6), T81–T95. https://doi.org/10.1190/1.2785046.

De Hoop, A.T., 1960. A modification of Cagniard's method for solving seismic pulse problems. Appl. Sci. Res. Sec. B 8 (1), 349–356. https://doi.org/10.1007/BF02920068.

Diaz, J., Ezziani, A., 2010. Analytical solution for waves propagation in heterogeneous acoustic/porous media. Part I: the 2D case. Commun. Comput. Phys. 7 (1), 171–194. https://doi.org/10.4208/cicp.2009.08.148.

Diaz, J., Ezziani, A., 2015. Gar6more2D (version 2.0). http://gar6more2d.gforge.inria.fr.

Etgen, J.T., 1986. High-order finite-difference reverse time migration with the 2-way non-reflecting wave equation. Stanford Explor. Project 133–146.

Fichtner, A., Hanasoge, S.M., 2017. Discrete wave equation upscaling. Geophys. J. Int. 209 (1), 353–357. https://doi.org/10.1093/gji/ggx016.

Fornberg, B., 1975. On a Fourier method for the integration of hyperbolic equations. SIAM J. Numer. Anal. 12 (4), 509–528. https://doi.org/10.1137/0712040.

Fryer, G.J., 1980. A slowness approach to the reflectivity method of seismogram synthesis. Geophys. J. Int. 63 (3), 747–758. https://doi.org/10.1111/j.1365-246X.1980.tb02649.x.

Fuchs, K., 1968. The reflection of spherical waves from transition zones with arbitrary depth-dependent elastic moduli and density. J. Phys. Earth 16 (Special), 27–41. https://doi.org/10.4294/jpe1952.16.Special_27.

Fuchs, K., Müller, G., 1971. Computation of synthetic seismograms with the reflectivity method and comparison with observations. Geophys. J. Int. 23 (4), 417–433. https://doi.org/10.1111/j.1365-246X.1971.tb01834.x.

Gallagher, J.W., Dromgoole, P.W., 2008. Seeing below the basalt – offshore Faroes. J. Article Geophys. Prospect. 56 (1), 33–45. https://doi.org/10.1111/j.1365-2478.2007.00670.x.

Gustafsson, B., Mossberg, E., 2004. Time compact high order difference methods for wave propagation. SIAM J. Sci. Comput. 26 (1), 259–271. https://doi.org/10.1137/030602459.

Gustafsson, B., Wahlund, P., 2004. time compact difference methods for wave propagation in discontinuous media. SIAM J. Sci. Comput. 26 (1), 272–293. https://doi.org/10.1137/S1064827503425900.

Gustafsson, B., Wahlund, P., 2005. time compact high order difference methods for wave propagation, 2D. J. Sci. Comput. 25 (1), 195–211. https://doi.org/10.1007/BF02728988.

Jones, I.F., Davison, I., 2014. Seismic imaging in and around salt bodies. Interpretation 2 (4), SL1–SL20. https://doi.org/10.1190/INT-2014-0033.1.

Juhlin, C., Young, R., 1993. Implications of thin layers for amplitude variation with offset (AVO) studies. Geophysics 58 (8), 1200–1204. https://doi.org/10.1190/1.1443504.

Kennett, B.L.N., 1974. Reflections, rays, and reverberations. Bull. Seismol. Soc. Am. 64 (6), 1685–1696. https://doi.org/10.1785/BSSA0640061685.

Kennett, B.L.N., 1979. Theoretical reflection seismograms for elastic media. Geophys. Prospect. 27 (2), 301–321. https://doi.org/10.1111/j.1365-2478.1979.tb00972.x.

Kennett, B.L.N., 2009. Seismic Wave Propagation in Stratified Media, New ed. ANU E Press, Canberra, ACT, Australia. https://doi.org/10.22459/SWPSM.05.2009.

Kosloff, D.D., Baysal, E., 1982. Forward modeling by a Fourier method. Geophysics 47 (10), 1402–1412. https://doi.org/10.1190/1.1441288.

Levander, A.R., 1988. Fourth-order finite-difference P-SV seismograms. Geophysics 53 (11), 1425–1436. https://doi.org/10.1190/1.1442422.

Lisitsa, V., Podgornova, O., Tcheverda, V., 2010. On the interface error analysis for finite difference wave simulation. Comput. Geosci. 14 (4), 769–778. https://doi.org/10.1007/s10596-010-9187-1.

Lombard, B., Piraux, J., 2004. Numerical treatment of two-dimensional interfaces for acoustic and elastic waves. J. Comput. Phys. 195 (1), 90–116. https://doi.org/10.1016/j.jcp.2003.09.024.

Mallick, S., Frazer, L.N., 1987. Practical aspects of reflectivity modeling. Geophysics 52 (10), 1355–1364. https://doi.org/10.1190/1.1442248.

Mavko, G., Mukerji, T., Dvorkin, J., 2009. The Rock Physics Handbook: Tools for Seismic Analysis of Porous Media. Cambridge University Press, Cambridge.

Mittet, R., 2017. On the internal interfaces in finite-difference schemes. Geophysics 82 (4), T159–T182. https://doi.org/10.1190/geo2016-0477.1.

Mittet, R., 2021a. On the pseudospectral method and spectral accuracy. Geophysics 86 (3), T127–T142. https://doi.org/10.1190/geo2020-0209.1.

Mittet, R., 2021b. Small-scale medium variations with high-order finite-difference and pseudospectral schemes. Geophysics 86 (5), T387–T399. https://doi.org/10.1190/geo2020-0210.1.

Moczo, P., Kristek, J., Vavrycuk, V., Archuleta, R.J., Halada, L., 2002. 3D heterogeneous staggered-grid finite-difference modeling of seismic motion with volume harmonic and arithmetic averaging of elastic moduli and densities. Bull. Seismol. Soc. Am. 92 (8), 3042–3066. https://doi.org/10.1785/0120010167.

Müller, G., 1985. The reflectivity method: a tutorial. J. Geophys. Zeitschrift für Geophysik 58, 153–174.

Müller, G., 2007. Theory of elastic waves, (Scientific Technical Report STR; 07/03), Potsdam : Deutsches GeoForschungsZentrum GFZ, p. 228. https://doi.org/10.2312/GFZ.b103-07037.

Pei, Z.-L., Fu, L.-Y., Yu, G.-X., Zhang, L.-X., 2009. A wavelet-optimized adaptive grid method for finite-difference simulation of wave propagation. Bull. Seismol. Soc. Am. 99 (1), 302–313. https://doi.org/10.1785/0120080002.

Raknes, E.B., Arntsen, B., Weibull, W., 2015. Three-dimensional elastic full waveform inversion using seismic data from the Sleipner area. Geophys. J. Int. 202 (3), 1877–1894. https://doi.org/10.1093/gji/ggv258.

Routh, P., Neelamani, R., Lu, R., Lazaratos, S., Braaksma, H., Hughes, S., Saltzer, R., Stewart, J., Naidu, K., Averill, H., Gottumukkula, V., Homonko, P., Reilly, J., Leslie, D., 2017. Impact of high-resolution FWI in the Western Black Sea: Revealing overburden and reservoir complexity. Lead. Edge 36 (1), 60–66. https://doi.org/10.1190/tle36010060.1.

Scheiber-Enslin, S.E., Manzi, M., Webb, S.J., 2021. Seismic imaging of dolerite sills and volcanic vents in the Central Karoo, South Africa: implications for shale gas potential. S. Afr. J. Geol. 124 (2), 465–480. https://doi.org/10.25131/sajg.124.0043.

Stephen, R.A., 1983. A comparison of finite difference and reflectivity seismograms for marine models. Geophys. J. Int. 72 (1), 39–57. https://doi.org/10.1111/j.1365-246X.1983.tb02803.x.

Symes, W.W., Vdovina, T., 2009. Interface error analysis for numerical wave propagation. Comput. Geosci. 13 (3), 363–371. https://doi.org/10.1007/s10596-008-9124-8.

Symes, W.W., Terentyev, I.S., Vdovina, T.W., 2008. Gridding requirements for accurate finite difference simulation. In: SEG Technical Program Expanded Abstracts, 2008, pp. 2077–2081. https://doi.org/10.1190/1.3059300.

Thomson, W.T., 1950. Transmission of elastic waves through a stratified solid medium. J. Appl. Phys. 21 (2), 89–93. https://doi.org/10.1063/1.1699629.

Tsvankin, Ilya, 1995. Seismic wavefields in layered isotropic media. Samizdat Press, Colorado School of Mines, Golden, CO.

Vishnevsky, D., Lisitsa, V., Tcheverda, V., Reshetova, G., 2014. Numerical study of the interface errors of finite-difference simulations of seismic waves. Geophysics 79 (4), T219–T232. https://doi.org/10.1190/geo2013-0299.1.

Warner, M., Ratcliffe, A., Nangoo, T., Morgan, J., Umpleby, A., Shah, N., Vinje, V., Štekl, I., Guasch, L., Win, C., Conroy, G., Bertrand, A., 2013. Anisotropic 3D full-waveform inversion. Geophysics 78 (2), R59–R80. https://doi.org/10.1190/geo2012-0338.1.

Widess, M.B., 1973. How thin is a thin bed? Geophysics 38 (6), 1176–1180. https://doi.org/10.1190/1.1440403.

Yao, G., da Silva, N.V., Debens, H.A., Wu, D., 2018. Accurate seabed modeling using finite difference methods. Comput. Geosci. 22 (2), 469–484. https://doi.org/10.1007/s10596-017-9705-5.

Zhang, C., Le Veque, R.J., 1997. The immersed interface method for acoustic wave equations with discontinuous coefficients. Wave Motion 25 (3), 237–263. https://doi.org/10.1016/S0165-2125(97)00046-2.

Zhang, C., Zhang, W., 2022. Efficient 2D acoustic wave finite-difference numerical simulation in strongly heterogeneous media using the adaptive mesh refinement technique. Geophysics 87 (1), T29–T42. https://doi.org/10.1190/geo2020-0801.1.

Zhang, Y., Zhang, H., Zhang, G., 2011. A stable TTI reverse time migration and its implementation. Geophysics 76 (3). https://doi.org/10.1190/1.3554411. WA3–WA11.